Article

Numerical Analysis of a High-Pressure Spatial Chemical Vapor Deposition (HPS-CVD) Reactor for Flow Stability at High Pressures

Hooman Enayati [ID] and Siddha Pimputkar *[ID]

Department of Materials Science and Engineering, Center for Photonics and Nanoelectronics, Lehigh University, Bethlehem, PA 18015, USA; hoe222@lehigh.edu
* Correspondence: sip516@lehigh.edu

Abstract: Highly indium-rich group-III nitrides are attracting attention for advancing our capacity to create highly effective optical emitters at extended visible/IR wavelengths or for enhancing bandgap engineering possibilities within the group-III nitride material framework. Current methods of synthesis are constrained in their efficacy, partially owing to the low decomposition temperature of indium nitride. Implementation of a new design of a vertical high-pressure spatial chemical vapor deposition (HPS-CVD) reactor with six separated precursor source zones and a rotating wafer carrier disk carrying four 2-inch wafers is proposed and analyzed using COMSOL Multiphysics as a commercial computational fluid dynamics (CFD) program to study the fluid phenomena inside the numerical domain. This study focuses on understanding the different flow patterns within the chambers at super-atmospheric conditions (5 atm to 30 atm) and identifying suitable operating conditions under which smooth and dominant vortex-free flow is achieved. Four 2-inch wafers are heated to maintain a temperature of 1200–1300 K at each pressure and gas type. Three different gas types (nitrogen, hydrogen, and ammonia) are used, and the impacts of different inlet flow velocities and rotational speeds are investigated and discussed. An operating matrix is presented for each analyzed system pressure providing suitable combinations of these operational variables for smooth flow in the chambers. Each gas type was identified to have a range of suitable rotational and inlet velocity regimes at each operating pressure. Overlap of these three gas-specific operating condition windows resulted in the identification of a generally suitable operating condition for smooth flow patterns in the system regardless of the gas type used, as required for the growth of group-III nitride materials.

Keywords: metal–organic chemical vapor deposition; semiconductor; computational fluid dynamics; turbulent flow modeling

1. Introduction

The semiconductor industry has relied upon advances in equipment development to enable new processes and materials with unprecedented controls or capabilities. One area that is critical to enabling devices is the thin-film growth process, which has the ability to deposit films of controlled composition and morphology. Metal–organic chemical vapor deposition (MOCVD) is a widely utilized industrial technique used for the manufacturing of electronic and optoelectronic devices such as light-emitting diodes (LEDs) or electronic devices based on compound semiconductors and the use of heterostructures [1–6].

The group-III nitride material family, including aluminum nitride (AlN), indium nitride (InN), and gallium nitride (GaN), has been well-established as III-V materials in the semiconductor industry. This is in large part due to their direct and wide bandgaps that enable them to absorb or emit light at UV/visible wavelengths and provide an avenue for more powerful power electronics. Of the three materials, InN is arguably the hardest to synthesize due to the relatively small decomposition temperature (~560 °C at 1 atm of

nitrogen) requiring lower growth temperatures to increase its incorporation into the film, leading to desired alloy compositions [7,8]. The common approach to achieve growth of $In_xGa_{1-x}N$ and $Al_{1-x}In_xN$ is to reduce the growth temperature up to the point at which the adatom mobility on the surface of the crystal becomes detrimental to the associated crystal quality. This tactic has allowed for the growth of relatively high-quality films of up to 25% indium in $In_{1-x}Ga_xN$ [9,10] or 17% indium in $Al_xIn_{1-x}N$ films [11,12]. Higher indium incorporation typically sees rapid deterioration of the crystal quality, leading to inefficient optical emitters. To mitigate problems resulting from the lower temperature growth of indium-containing III-Ns, improved understandings of precursor chemistries and gas-phase reactions are being investigated [13–16].

To improve the crystal quality of high-indium-content films and potentially reduce associated point defects, higher growth temperatures are desired. Growth of these materials at higher pressures offers a viable path. By increasing the pressure of nitrogen-containing molecules during the growth of these group-III nitrides, the increased nitrogen activity stabilizes the material, leading to increased decomposition temperatures. Woods [17] concluded that InN could be grown at ~1275 K for a system at ~70 atm. It was also shown that stable growth of the high-In-content $In_{1-x}Ga_xN$ films is possible where x < 0.65.

Efforts have been made to develop high-pressure horizontal MOCVD systems permitting access to operating under 10 s of atmospheres or pressure [18–21]. However, due to fluid dynamics limitations, actual operating pressures were limited to ~15 atm due to the onset of turbulence and precursor loss from the flow due to enhanced precursor interactions with themselves and the walls, leading to slow growth rates of ~200 nm/hr and subpar film quality [22].

To address the known limitations of high-pressure MOCVDs, a new CVD reactor design has been proposed that minimizes precursor pre-reactions through spatial separation while also providing optimal fluid dynamics for controlled synthesis of thin films [23]. The design of the reactor must consider fluid dynamics and mass transport to ensure high film quality, uniformity, and deposition rates. A successful CVD reactor design for controlled thin film synthesis should achieve a stable and vortex-free flow pattern under optimal conditions. Computational fluid dynamics (CFD) as a foretelling means has made a significant contribution in simulating actual flow and thermal studies, thereby eliminating the need for expensive and time-consuming physical experiments.

Several researchers have used numerical models to analyze CVD reactors [24–44]. As an example, He et al. [45] used machine learning and the PSO algorithm to conduct a numerical simulation of a MOCVD and found that the flow ratio of the source's inlets did not have a significant effect on flow states in general.

This paper discusses the design and CFD-based optimization of a new super-atmospheric, vertical MOCVD reactor with spatially separated precursor zones, referred to as a high-pressure spatial CVD (HPS-CVD) reactor. The current authors reported on a systematic study of this reactor in a publication analyzing the performance of this reactor at one atmospheric pressure [46]. They explored the effects of the inlet velocity, inlet chamber area, rotational speed of the susceptor, and turbulent model on the flow behavior within the chamber.

2. Scope of Work

This article is a continuation of the previous study discussed in [46], wherein the authors investigate the flow patterns of ammonia, hydrogen, and nitrogen in a vertical MOCVD reactor. The objectives of this study for operating pressures greater than 1 atm up to 30 atm are (i) to identify smooth flow regimes inside the reactor chambers by selecting appropriate rotational speeds and inlet velocity values while maintaining the wafer temperature within the range of 1200–1300 K and (ii) to define an operating condition matrix (rotational speed (rpm) vs. inlet flow velocity) to provide a basis for future experimental studies.

3. Governing Equations

The equations that governed the current investigation are the steady, compressible Navier–Stokes equations, which consider temperature-dependent properties from the COMSOL material library. The continuity, momentum, and energy equations are presented in [47]. The general properties of nitrogen, hydrogen, and ammonia can be found in [48–51].

4. Numerical Method

4.1. Geometry and Corresponding Numerical Domain

This study focuses on a vertical HPS-CVD reactor equipped with a rotating wafer carrier disk, as illustrated in Figure 1a in [46]. The design of this reactor minimizes the pre-reactions of the precursors and mitigates their interaction to the period of diffusion through the boundary layer. A flattened and linear presentation of the circular shape of the barrier, boundary layer, and rotational disk can be seen in Figure 1 of [23] for better understanding.

The reactor is composed of various components including a shroud, six chambers, and a wafer carrier disk that accommodates multiple wafers, heaters, insulated zones, susceptors, a disk, and a shaft (refer to Figure 1b,c in [46]). The reactor has six independent precursor zones separated by barriers and a mixing layer where deposition occurs. The mixing layer is filled with fluid located between the barrier and the rotating carrier disk. Each chamber is connected to a dedicated gas source that provides a gas mixture with group-III elements, nitrogen-containing species, inert gases, or dopants precursors, as per user specification. In this design, the present gap between the top of the wafer carrier disk and the lower part of the barrier is 0.12 inches.

As the reactor used in this study is identical to the one presented in [46], details regarding the dimensions and other geometrical features of the reactor can be found there. The working fluid (nitrogen/hydrogen/ammonia) is considered Newtonian, compressible, and to have temperature-dependent properties.

The numerical simulation encompasses both fluid and solid domains. The fluid region is enclosed by the walls of the shroud and carrier disk. The shroud is constructed with a thickness of 4 mm using molybdenum material. The carrier disk comprises multiple solid domains, and the working fluid is in contact with the external surface of some of these domains (such as the wafer, shaft, thermal insulator, and disk sections shown in Figure 1c in [46]). The properties of all the solid domains are provided in Table 1 in [46]. The working fluid enters the system through six inlets, traverses the chambers, and subsequently flows within the gap (0.12 inches) formed between the rotating carrier disk and the barriers. This gap size was optimized (ranging from 0.06–0.18 inches) to get the best possible flow pattern while considering unchanged boundary conditions. Finally, the working fluid exits the domain through the outlet/exhaust.

The numerical domain is discretized to form a grid of elements. Similar to the study presented in [46], an unstructured mesh was used with approximately 2.3 million elements. Notably, the grid is refined in close proximity to the walls to effectively resolve the boundary layers, as depicted in Figure 3b in [46].

In all numerical simulations conducted in this research study, the authors accounted for all three modes of heat transfer: conduction, convection, and radiation. In systems characterized by high temperatures (i.e., T > 1000 K), radiation plays a significant role in heat transfer. Therefore, it was crucial to incorporate radiative heat flux in the numerical modelling of this HPS-CVD reactor. Heat conduction primarily governs heat transfer in solids, while convection comes into play when simulating fluid domains. Within the domain, pockets of flow facilitate energy exchange through internal movements. For further details, additional information can be found in reference books focusing on heat transfer.

For MOCVD reactors, where the Reynolds number criterion lacks clarity and the reactor design incorporates irregular corners, turbulent flow is expected considering the different gas inlet magnitude and rotational speed. Hence, a turbulent flow model in COMSOL Multiphysics [47] was utilized to accurately depict the flow patterns within the

reactor. It is worth noting that a turbulent model can handle laminar flows if the minimum required mesh density is met, thus obviating the necessity for a laminar model.

Among the various turbulence models, the k-ω low-Re turbulence model stands out as one of the most frequently employed for analyzing turbulent flow conditions. This model is one type of the Reynolds-averaged Navier–Stokes (RANS) family of turbulence models, where turbulence effects are "modeled" rather than directly solved. The k-ω turbulence model comes in two variants: standard and shear stress transport (SST). The standard k-ω model exhibits superior performance for complex boundary layer flows subjected to adverse pressure gradients. On the other hand, the SST formulation transitions to a k-ϵ behavior (another type of RANS turbulent model) in the free-stream, thus mitigating the sensitivity to inlet free-stream turbulence properties observed with the k-ω model.

4.2. Boundary and Initial Conditions

This study presents steady-state calculations of fluid flow conducted within a reactor featuring a rotating disk. The initial conditions were set such as the numerical domain depicted in Figure 2a in [46] and had a constant temperature of 873.15 °C, with the working fluid initially at zero velocity. A good choice of initial temperature can accelerate the speed of a simulation. In Figure 1a [46], the outer walls of the chambers are subjected to radiation and forced convection, while the inner walls of the chambers trade heat through radiation. The radiative heat transfer is considered transparent for both the working fluid and the wafers. The chamber walls were assumed to have a no-slip condition. As for the carrier disk walls, which include the external surface of the wafers, thermal insulating areas, and the disk section, they were treated as moving walls due to the rotational speed, and the appropriate velocity treatment was applied to them. The pressure outlet was also placed at the chamber's exhaust. Further details regarding the default operating conditions used in all simulations of this paper can be found in Table 1.

Table 1. Parameters and their values in all models unless stated otherwise.

Parameter	Value (s)
Rotational speed (rpm)	50, 100, 200, 300, 400
Operating pressure (atm)	5, 10, 20, 30
Heat transfer coefficient (W/m^2·K)	50
Inlet velocity/chamber (m/s)	0.5–0.8
Inlet gas temperature (K)	298.15
Input power/wafer (watt)	Varied
Surrounding temperature (K)	298.15
Area per inlet (in^2)	0.1064
Molybdenum emissivity	0.1

4.3. Numerical Set Up

In accordance with Figure 3 in [46] and the description provided in Section 4.1, a non-structured and non-uniform grid was implemented. The governing equations with the specified initial and boundary conditions were solved numerically using COMSOL Multiphysics [47]. This commercial software employs the finite element method to discretize the governing equations. The momentum equation was discretized using the P1 + P1 method, while the energy equation was discretized using the linear method. In the present study, a direct solver was employed in a multi-step analysis due to its robustness, despite its higher RAM usage. A relative tolerance of 5×10^{-3} was applied in all solver steps.

4.4. Mesh Study

A study on mesh convergence was conducted using three distinct grids, consisting of 1.7 million, 2.3 million, and 4.1 million elements. The temperature of the fluid inside the reactor as well as of the wafers was monitored across all three grids. The measured percentage error between grids 2 and 3 was found to be below 5% in all locations.

Each simulation duration varied from 14 to 40 h on 32 cores of the Intel Xeon processor, depending on the operating pressure and density of the grid used in the calculations. Considering the outcomes of the mesh convergence study, the authors selected the 2.3 million-element grid size as the default and performed all simulations accordingly. The grid of 2.3 million elements comprised various types of elements, including tetrahedrons, quads, pyramids, prisms, triangles, and hexes. For a comprehensive overview, a detailed summary of the characteristics of the 2.3 million-element mesh is provided in Table 2.

Table 2. Mesh statistics considering 2.3 million elements.

Metric	Minimum Value	Average
Skewness	0.002	0.659
Growth rate	0.0	0.57
Maximum angle	0.05	0.77
Volume versus length	3.3×10^{-4}	0.49

5. Results and Discussion

This section presents an in-depth investigation of the flow patterns within the depicted geometric configuration shown in Figure 1 in [46], employing numerical analysis and investigations. The top view of the numerical domain, aligned parallel to the XY plane as depicted in Figure 1a in [41], is utilized to analyze flow patterns across the numerical domain. By analyzing the obtained data, a proposed range of operating conditions (for N_2 and H_2 at 5, 10, 20, and 30 atm and for NH_3 at 5 and 10 atm) is put forth to achieve smooth flow patterns inside the reactor while maintaining a minimum flow rate (slm). The streamlines in the chambers were evaluated quantitatively and qualitatively.

In Sections 5.1–5.3, the numerical outcomes for N_2, H_2, and NH_3, respectively, are showcased, considering various inlet velocities, rotational speeds, and operating pressures.

5.1. Nitrogen

This section focuses on the influence of changes in inlet velocity magnitude and rotational speed on the flow streamlines within chambers at 5 atm (presented in Figures 1–3, depicting a top view of the reactor). These figures illustrate the circulation of nitrogen in the numerical domain for three different rotational speeds (rpm) at 5 atm. Figure 1 displays the nitrogen circulation for a fixed rotational speed of 50 rpm (rotational speed of the carrier disk) and four different inlet velocity magnitudes: 0.5, 0.6, 0.7, and 0.8 m/s. It is important to note that the velocity streamlines in this figure (and all other similar figures of this article) are color-coded based on temperature, with the legend bar indicating higher temperatures in the red range and lower temperatures in the blue range.

As with the previous part of this system, present in [46], the current authors opted for total of 10,000 streamlines for the whole system to accurately capture the underlying physics of the fluid, considering its continuous nature. Increasing the number of streamlines enhances the fidelity of the simulated flow patterns. It is possible to employ a lower number of streamlines, 1000 as an example, but this may result in certain flow pattern details being overlooked.

Reviewing Figure 1, it becomes apparent that as the inlet speed goes up, the flow patterns become smoother over the majority of the wafers' area. This can be attributed to the balance between the inlet flow velocity and the rotational speed of the carrier disk, resulting in a weakened formation of vortices due to the momentum balance. Additionally, some localized disturbances can be observed in the center of the plots in Figure 1. As these small and localized chaotic movements do not significantly impact the overall flow patterns across the majority of the wafers' areas, the authors consider them to be minor deviations. It should be noted that these small areas are predominantly visible when using a total of 10,000 streamlines within the system. By reducing the number of streamlines, the disturbances become minimal and typically are eliminated from view.
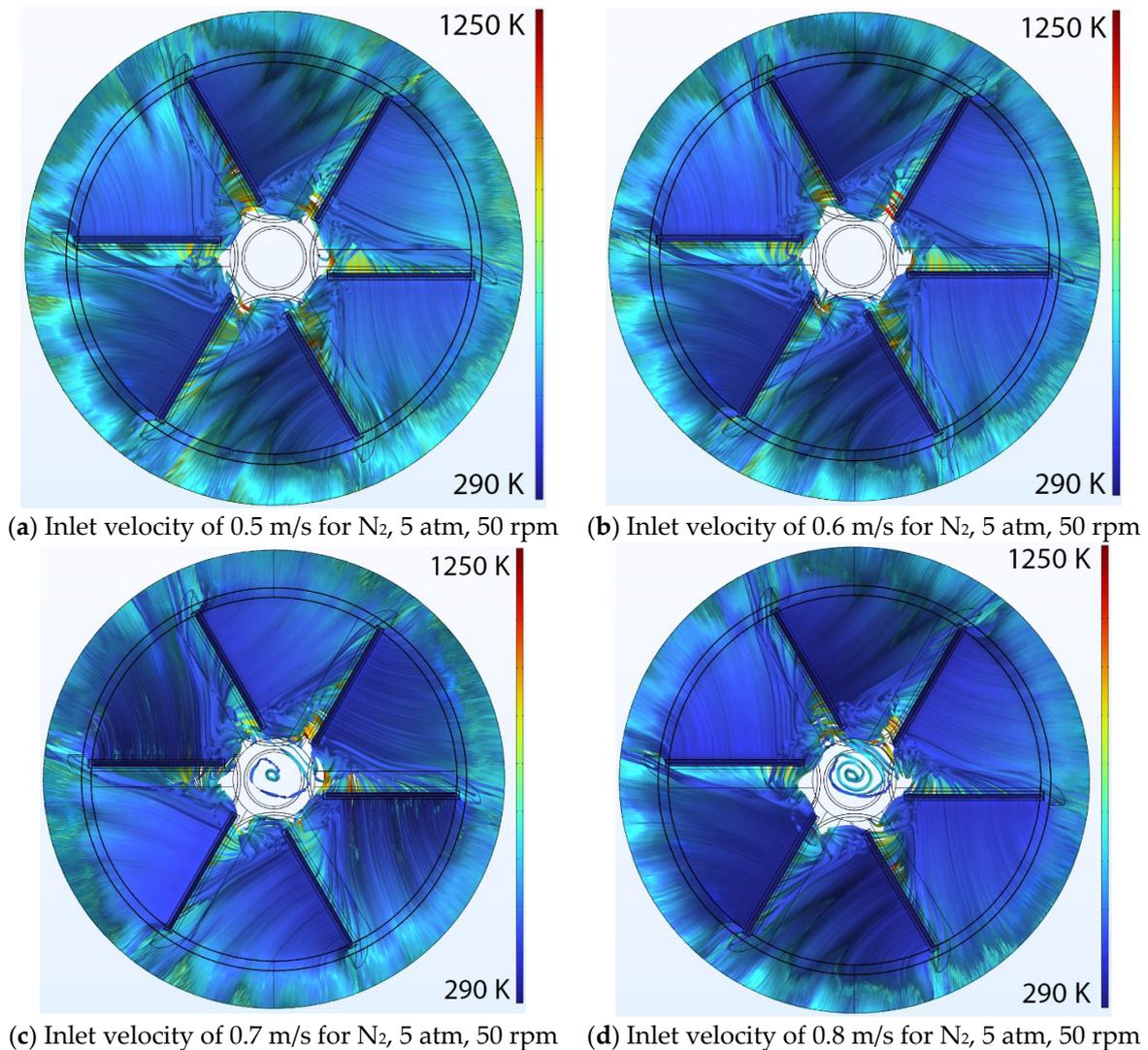
(**a**) Inlet velocity of 0.5 m/s for N_2, 5 atm, 50 rpm　(**b**) Inlet velocity of 0.6 m/s for N_2, 5 atm, 50 rpm

(**c**) Inlet velocity of 0.7 m/s for N_2, 5 atm, 50 rpm　(**d**) Inlet velocity of 0.8 m/s for N_2, 5 atm, 50 rpm

Figure 1. A top-down depiction showing 10,000 velocity streamlines color-coded according to temperature within the chambers, under the conditions of N_2 at 5 atm pressure. The disk rotates at 50 rpm, while gas is introduced at inlet velocities of (**a**) 0.5 m/s, (**b**) 0.6 m/s, (**c**) 0.7 m/s, and (**d**) 0.8 m/s. Gas temperature is consistently color-coded across all panels, varying from 290 K (blue) to 1250 K (red).

Figures 2 and 3 present comparable data sets for nitrogen at the operating pressure of 5 atm, with rotational speeds of 100 rpm and 200 rpm, respectively. Similarly in Figure 1, the observation drawn from the data is that as the inlet velocity increases, the streamlines appear noticeably more streamlined.

In line with the previous study [46], the current authors incorporated a pass/fail standard to evaluate flow patterns within the numerical domain. It is noteworthy that the objective was to identify the smoothest flow patterns on top of the wafer, and out of the 10,000 streamlines examined, not all inlet velocity values met the passing criterion. The authors adopted the same failing/passing criterion (more than one bad streamline in 10,000 streamlines as failing) as in [46] and provide a summary of the pass/fail results for nitrogen at an operating pressure of 5 atm, along with the corresponding rotational speeds, in Table 3. In Table 3, a cross mark indicates a failure, while a checkmark represents a pass. A greyed background against a checkmark indicates simultaneous passing conditions for all three gases of the system.

(**a**) Inlet velocity of 0.5 m/s for N_2, 5 atm, 100 rpm   (**b**) Inlet velocity of 0.6 m/s for N_2, 5 atm, 100 rpm

(**c**) Inlet velocity of 0.7 m/s for N_2, 5 atm, 100 rpm   (**d**) Inlet velocity of 0.8 m/s for N_2, 5 atm, 100 rpm

Figure 2. A top-down depiction showing 10,000 velocity streamlines color-coded according to temperature within the chambers, under the conditions of N_2 at 5 atm pressure. The disk rotates at 100 rpm, while gas is introduced at inlet velocities of (**a**) 0.5 m/s, (**b**) 0.6 m/s, (**c**) 0.7 m/s, and (**d**) 0.8 m/s. Gas temperature is consistently color-coded across all panels, varying from 300 K (blue) to 1213 K (red).

Table 3. Pass/fail assessment of conditions for N_2 across various operating pressures, rotational speeds, and inlet speeds. Failing conditions are denoted by red cross marks, while passing conditions are indicated by green checkmarks, according to the criterion of no more than 1 'bad' streamline out of 10,000. Passing criteria for all gases under the same conditions are shown up in grey.

N_2	System Pressure (atm)											
	5			10			20			30		
Inlet Speed (m/s)	Rotational Speed of Disc (rpm)											
	50	100	200	100	200	300	200	300	400	200	300	400
0.5	✗	✗	✗	✗	✗	✗	✗	✗	✗	✗	✗	✗
0.6	✗	✗	✗	✗	✗	✗	✓	✓	✓	✗	✗	✗
0.7	✓	✓	✓	✓	✓	✓	✓	✓	✓	✗	✗	✓
0.8	✓	✓	✓	✓	✗	✓	✗	✓	✓	✗	✗	✓

(**a**) Inlet velocity of 0.5 m/s for N_2, 5 atm, 200 rpm   (**b**) Inlet velocity of 0.6 m/s for N_2, 5 atm, 200 rpm

(**c**) Inlet velocity of 0.7 m/s for N_2, 5 atm, 200 rpm   (**d**) Inlet velocity of 0.8 m/s for N_2, 5 atm, 200 rpm
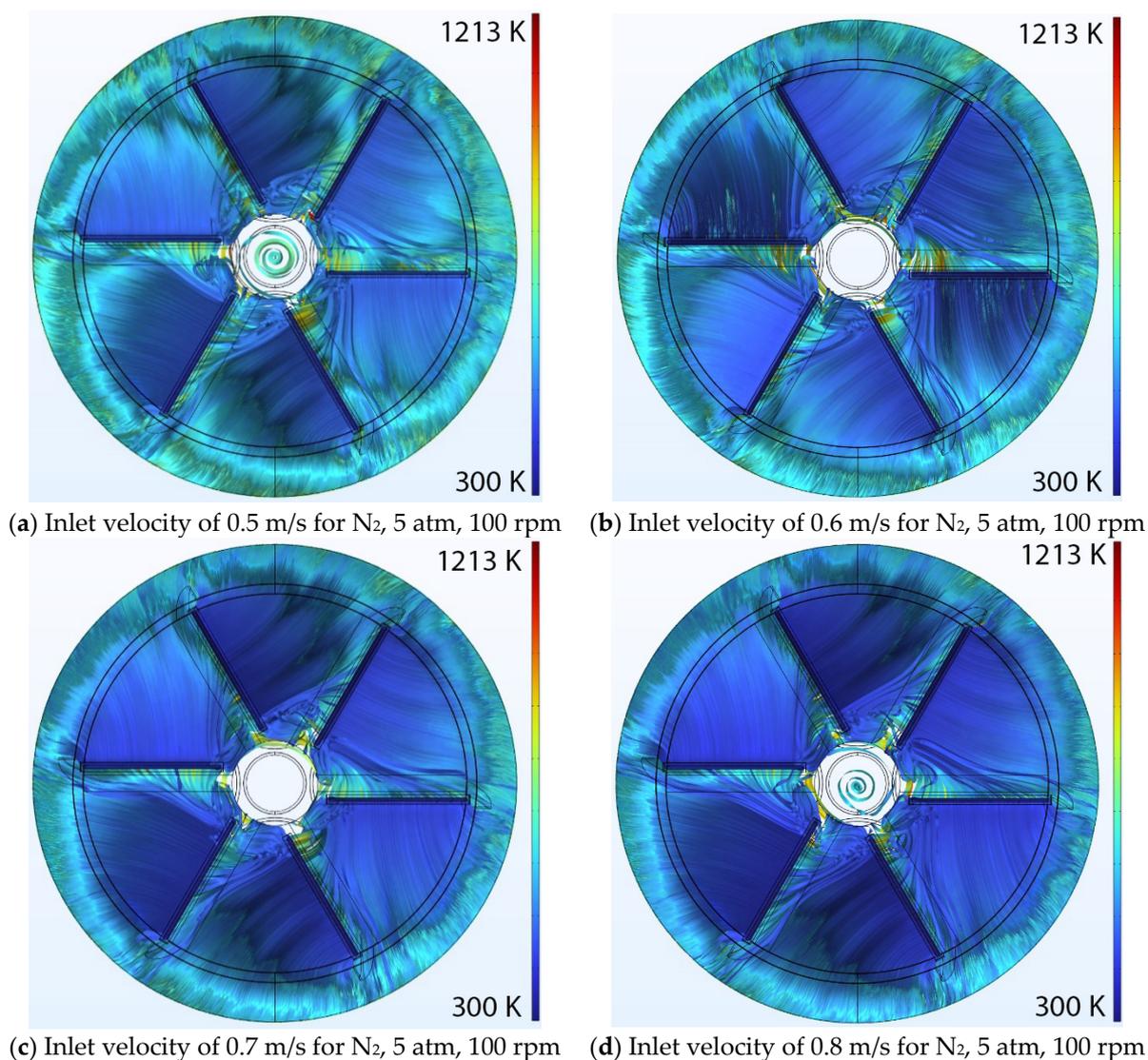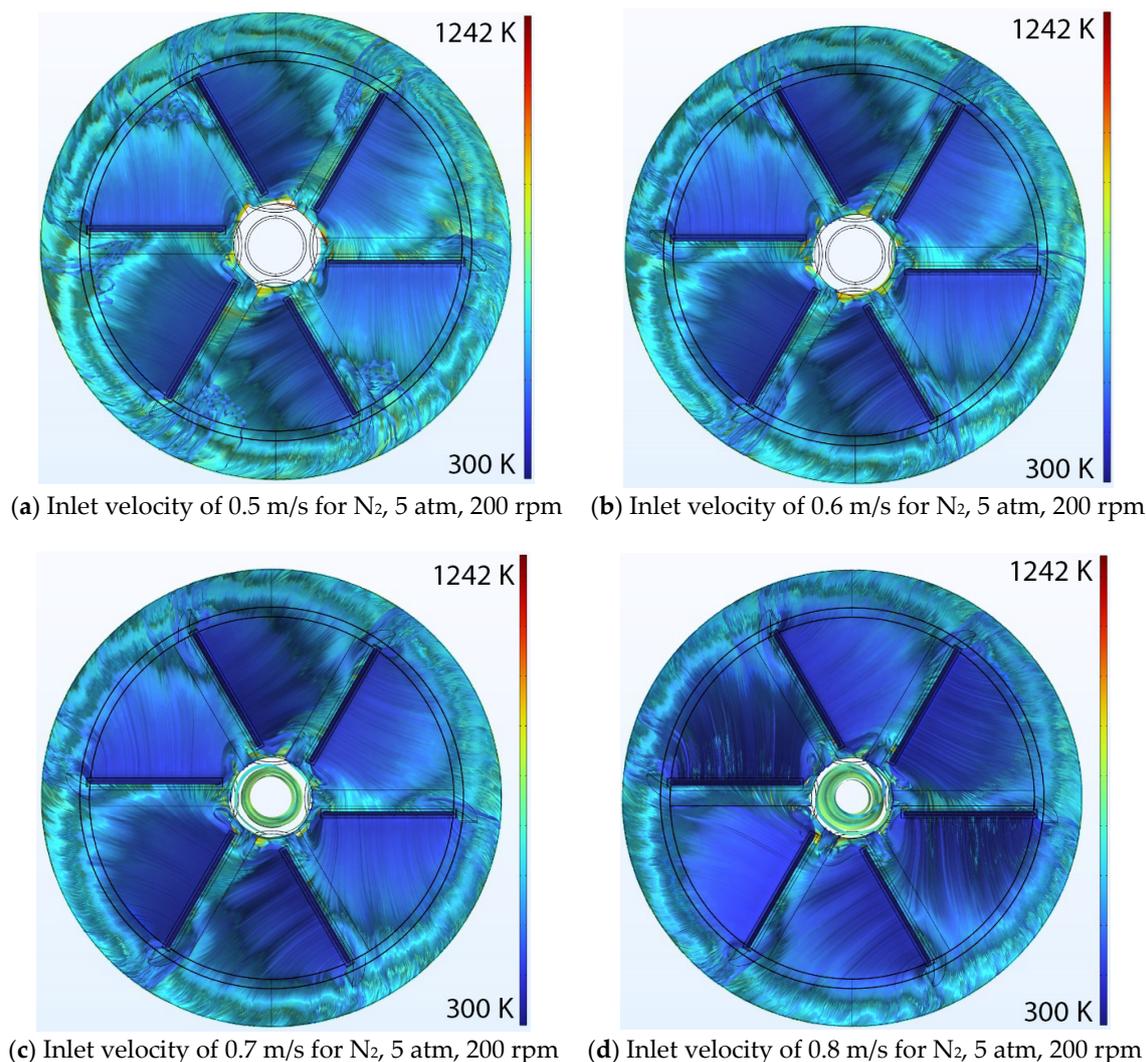
Figure 3. A top-down depiction showing 10,000 velocity streamlines color-coded according to temperature within the chambers, under the conditions of N_2 at 5 atm pressure. The disk rotates at 200 rpm, while gas is introduced at inlet velocities of (**a**) 0.5 m/s, (**b**) 0.6 m/s, (**c**) 0.7 m/s, and (**d**) 0.8 m/s. Gas temperature is consistently color-coded across all panels, varying from 300 K (blue) to 1242 K (red).

Based on the data presented in Table 3, it is evident that an inlet velocity of either 0.7 m/s or 0.8 m/s is required at all rotational speeds to achieve a smooth flow on the surface of the wafers and meet the defined pass/fail criterion for an operating pressure of 5 atm. Given that lower flow rates and rotational speeds are preferable, it can be inferred that nitrogen at 5 atm would necessitate an inlet velocity of 0.7 m/s for optimal performance within the chambers.

The same methodology was applied to nitrogen at higher pressures of 10, 20, and 30 atm to determine the range of inlet velocity magnitudes and rotational speeds that would result in smooth flow patterns with minimal disruption on the surface of the wafers. By employing the identical pass/fail criterion, the authors compiled the data and present it in Table 3. Visual representations of the progression of flow pattern figures for nitrogen at higher pressures are made available in the supplementary document (Section S1 and Figures S1–S9).

In general, two regimes were found to exist with respect to pressure. At pressures at and below 20 atm, the system exhibits a relatively large operating window for higher inlet velocities with a wide range of acceptable combinations between disk rotation speed and inlet velocities. With increasing pressure, a need to increase the rotational speed was

found to be necessary to stabilize the flow. Going from 10 atm to 20 atm, the increased momentum coming from the inlet flow at these pressures appeared to stabilize the low pattern at lower inlet velocities. At 30 atm, higher rotational speeds and inlet velocities were needed to avoid the onset of vortex generation and poorer flow conditions in the individual chambers.

5.2. Hydrogen

The numerical results of various operating pressures inside the numerical domain using hydrogen as the working fluid are presented in this section. Figures 4–6 present comparable information as in Figures 1–3 but for hydrogen as the working fluid. The defaulting number of 10,000 velocity streamlines, temperature color-coded, was implemented to depict the flow patterns in the numerical chambers. As can be understood, the chaotic gas flow movements in the chamber became weak as the inlet gas speed increased from 0.5 to 0.8 m/s. By applying the identical passing/failing criterion, the results for hydrogen at 5 atm and various rotational speeds are condensed and presented in Table 4. Visual representations of the progression of flow patterns figures for hydrogen at higher pressures are made available in the supplementary document (Section S2 and Figures S10–S18), and the pass/fail criteria are provided in Table 4.

(**a**) Inlet velocity of 0.5 m/s for H_2, 5 atm, 50 rpm   (**b**) Inlet velocity of 0.6 m/s for H_2, 5 atm, 50 rpm

(**c**) Inlet velocity of 0.7 m/s for H_2, 5 atm, 50 rpm   (**d**) Inlet velocity of 0.8 m/s for H_2, 5 atm, 50 rpm

Figure 4. A top-down depiction showing 10,000 velocity streamlines color-coded according to temperature within the chambers, under the conditions of H_2 at 5 atm pressure. The disk rotates at 50 rpm, while gas is introduced at inlet velocities of (**a**) 0.5 m/s, (**b**) 0.6 m/s, (**c**) 0.7 m/s, and (**d**) 0.8 m/s. Gas temperature is consistently color-coded across all panels, varying from 300 K (blue) to 1227 K (red).

(**a**) Inlet velocity of 0.5 m/s for H$_2$, 5 atm, 100 rpm   (**b**) Inlet velocity of 0.6 m/s for H$_2$, 5 atm, 100 rpm

(**c**) Inlet velocity of 0.7 m/s for H$_2$, 5 atm, 100 rpm   (**d**) Inlet velocity of 0.8 m/s for H$_2$, 5 atm, 100 rpm
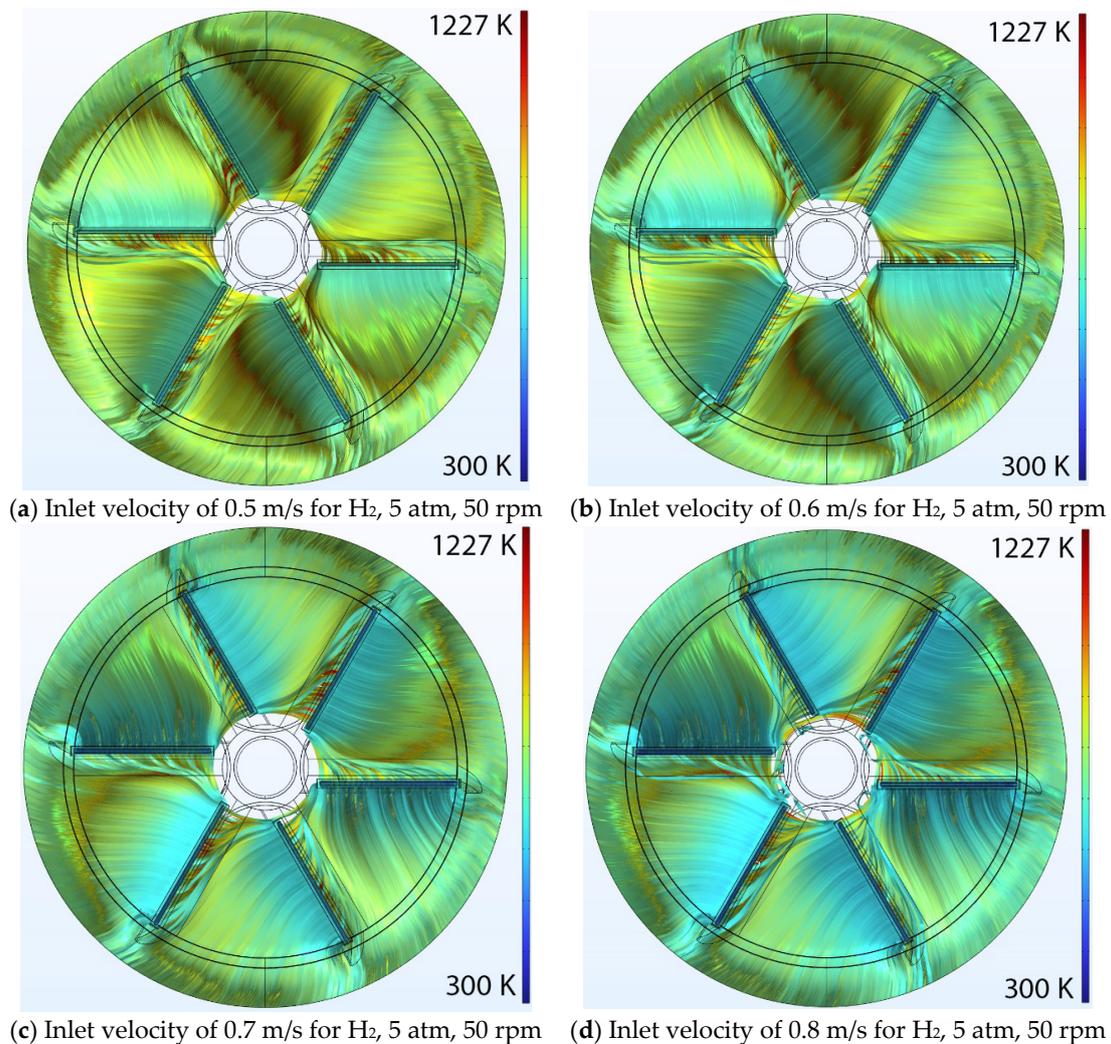
Figure 5. A top-down depiction showing 10,000 velocity streamlines color-coded according to temperature within the chambers, under the conditions of H$_2$ at 5 atm pressure. The disk rotates at 100 rpm, while gas is introduced at inlet velocities of (**a**) 0.5 m/s, (**b**) 0.6 m/s, (**c**) 0.7 m/s, and (**d**) 0.8 m/s. Gas temperature is consistently color-coded across all panels, varying from 300 K (blue) to 1245 K (red).

Table 4. Pass/fail assessment of conditions for H$_2$ across various operating pressures, rotational speeds, and inlet speeds. Failing conditions are denoted by red cross marks, while passing conditions are indicated by green checkmarks, according to the criterion of no more than 1 'bad' streamline out of 10,000. Passing criteria for all gases under the same conditions are shown up in grey.

H$_2$	System Pressure (atm)											
	5			10			20			30		
Inlet Speed (m/s)	Rotational Speed of Disc (rpm)											
	50	100	200	100	200	300	200	300	400	200	300	400
0.5	✗	✗	✗	✗	✗	✗	✗	✗	✗	✓	✓	✗
0.6	✓	✗	✗	✗	✗	✗	✗	✗	✗	✓	✓	✗
0.7	✓	✓	✗	✓	✗	✗	✗	✗	✗	✓	✓	✓
0.8	✓	✗	✗	✓	✗	✗	✓	✓	✗	✓	✓	✓

(**a**) Inlet velocity of 0.5 m/s for H$_2$, 5 atm, 200 rpm (**b**) Inlet velocity of 0.6 m/s for H$_2$, 5 atm, 200 rpm

(**c**) Inlet velocity of 0.7 m/s for H$_2$, 5 atm, 200 rpm (**d**) Inlet velocity of 0.8 m/s for H$_2$, 5 atm, 200 rpm
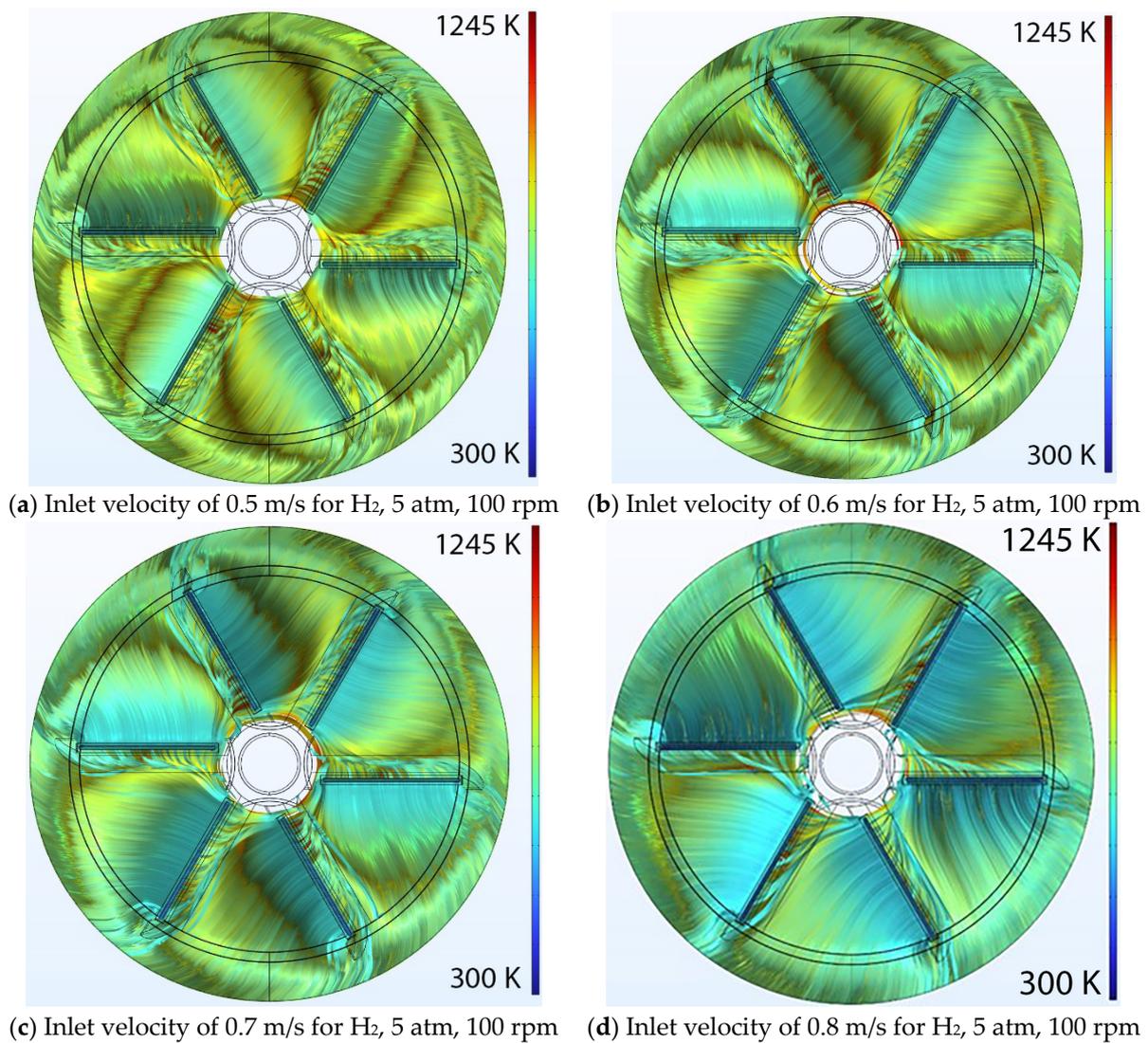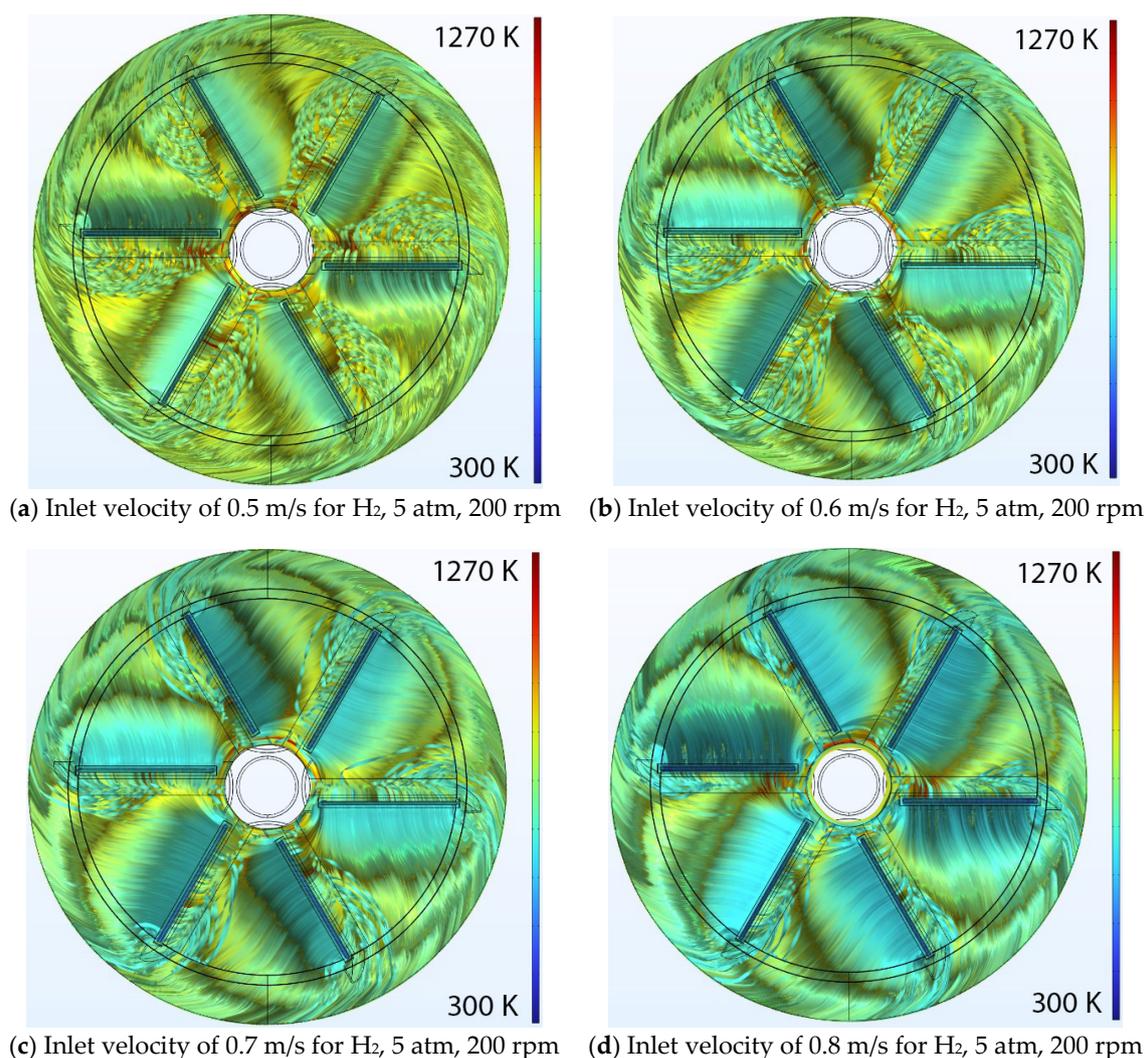
Figure 6. A top-down depiction showing 10,000 velocity streamlines color-coded according to temperature within the chambers, under the conditions of H$_2$ at 5 atm pressure. The disk rotates at 200 rpm, while gas is introduced at inlet velocities of (**a**) 0.5 m/s, (**b**) 0.6 m/s, (**c**) 0.7 m/s, and (**d**) 0.8 m/s. Gas temperature is consistently color-coded across all panels, varying from 300 K (blue) to 1270 K (red).

Table 4 reveals that similar to nitrogen, higher rotational speeds are needed to stabilize the flow pattern in the system. Smaller operating windows were found for hydrogen and can be traced back to the lighter molecules, resulting in a lower momentum contribution to the flow. In particular, the system is less flexible to accommodate higher rotational speeds of the disk, leading to the onset of vortices. As the system transitions from 20 atm to 30 atm, as with nitrogen gas, the system undergoes a transition in stability for the flow. Contrary to the nitrogen case in which the system becomes overall less stable, enhanced stability is observed for the gas of hydrogen, allowing for a large operating window with reduced inlet velocities and rotational speeds yielding stable flow patterns.

These results, when combined with the observed nitrogen behavior, suggests that a hydrogen–nitrogen gas blend in which the properties are graded from the two pure gas endpoints may stabilize the system over a wide range of operating conditions at all pressures.

5.3. Ammonia

Ammonia, chosen as the third working fluid, was utilized to explore the flow and thermal patterns within the computational domain. Like in Sections 5.1 and 5.2, the authors

examined various flow patterns at different inlet velocities and rotational speeds to identify the most favorable conditions for achieving smooth flow patterns over the wafer. Contrary to nitrogen and hydrogen, for which the data were sourced from the internal COMSOL library for the properties, the properties of ammonia were taken from the National Institute of Standards and Technology (NIST) webpage and from [42] to allow for an assessment of this system at higher pressures. Ammonia was only investigated up to a pressure of 10 atm, as it is anticipated that it would condense in the system and supply lines feeding the system above these values due to its liquid/gas transition pressure of 10.5 atm at 300 K.

Similar to the previous figures, Figures 7–9 illustrate the flow pattern within the numerical domain from a top view, utilizing 10,000 temperature color-coded streamlines for three different rpms: 50, 100, and 200 at 5 atm. Employing a similar approach as in the previous sections and using comparable criteria, it is feasible to establish a range of inlet velocities and rotational speeds for ammonia at 5 atm. This range ensures the formation of minimal vortices within the numerical domain, and the results are summarized in Table 5. Supplementary figures (Section S3 and Figures S19–S21) illustrating ammonia streamline patterns at 10 atm can be found in the supplementary section of this article, and the pass/fail criteria outcomes are included in Table 5.

(**a**) Inlet velocity of 0.5 m/s for NH₃, 5 atm, 50 rpm (**b**) Inlet velocity of 0.6 m/s for NH₃, 5 atm, 50 rpm

(**c**) Inlet velocity of 0.7 m/s for NH₃, 5 atm, 50 rpm (**d**) Inlet velocity of 0.8 m/s for NH₃, 5 atm, 50 rpm

Figure 7. A top-down depiction showing 10,000 velocity streamlines color-coded according to temperature within the chambers, under the conditions of NH₃ at 5 atm pressure. The disk rotates at 50 rpm, while gas is introduced at inlet velocities of (**a**) 0.5 m/s, (**b**) 0.6 m/s, (**c**) 0.7 m/s, and (**d**) 0.8 m/s. Gas temperature is consistently color-coded across all panels, varying from 300 K (blue) to 1242 K (red).

(**a**) Inlet velocity of 0.5 m/s for NH₃, 5 atm, 100 rpm
(**b**) Inlet velocity of 0.6 m/s for NH₃, 5 atm, 100 rpm

(**c**) Inlet velocity of 0.7 m/s for NH₃, 5 atm, 100 rpm
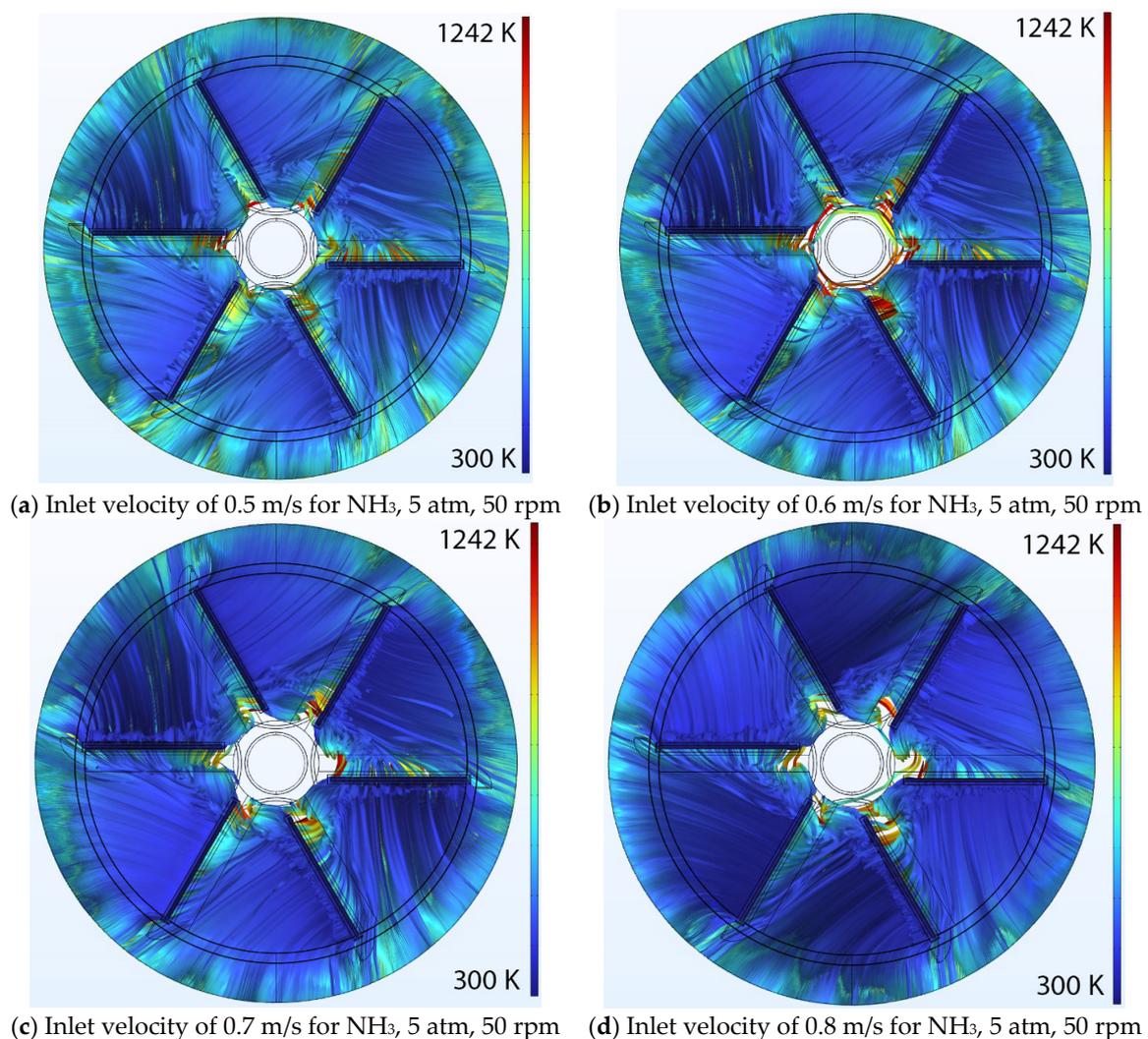(**d**) Inlet velocity of 0.8 m/s for NH₃, 5 atm, 100 rpm

Figure 8. A top-down depiction showing 10,000 velocity streamlines color-coded according to temperature within the chambers, under the conditions of NH_3 at 5 atm pressure. The disk rotates at 100 rpm, while gas is introduced at inlet velocities of (**a**) 0.5 m/s, (**b**) 0.6 m/s, (**c**) 0.7 m/s, and (**d**) 0.8 m/s. Gas temperature is consistently color-coded across all panels, varying from 300 K (blue) to 1250 K (red).

Table 5. Assessment of pass/fail operating conditions for NH_3 across varying operating pressures, rotational speeds, and inlet speeds. Failing conditions are indicated by red cross marks, while passing conditions are denoted by green checkmarks, adhering to the specified criterion of no more than 1 'bad' streamline out of 10,000 streamlines. Passing criteria for all gases under the same conditions are shown in grey.

NH_3	System Pressure (atm)					
	5			10		
Inlet Speed (m/s)	Rotational Speed of Disc (rpm)					
	50	100	200	100	200	300
0.5	✘	✘	✘	✘	✘	✘
0.6	✘	✘	✔	✘	✘	✘
0.7	✘	✘	✔	✘	✘	✔
0.8	✔	✔	✔	✔	✘	✔

(**a**) Inlet velocity of 0.5 m/s for NH₃, 5 atm, 200 rpm   (**b**) Inlet velocity of 0.6 m/s for NH₃, 5 atm, 200 rpm

(**c**) Inlet velocity of 0.7 m/s for NH₃, 5 atm, 200 rpm   (**d**) Inlet velocity of 0.8 m/s for NH₃, 5 atm, 200 rpm
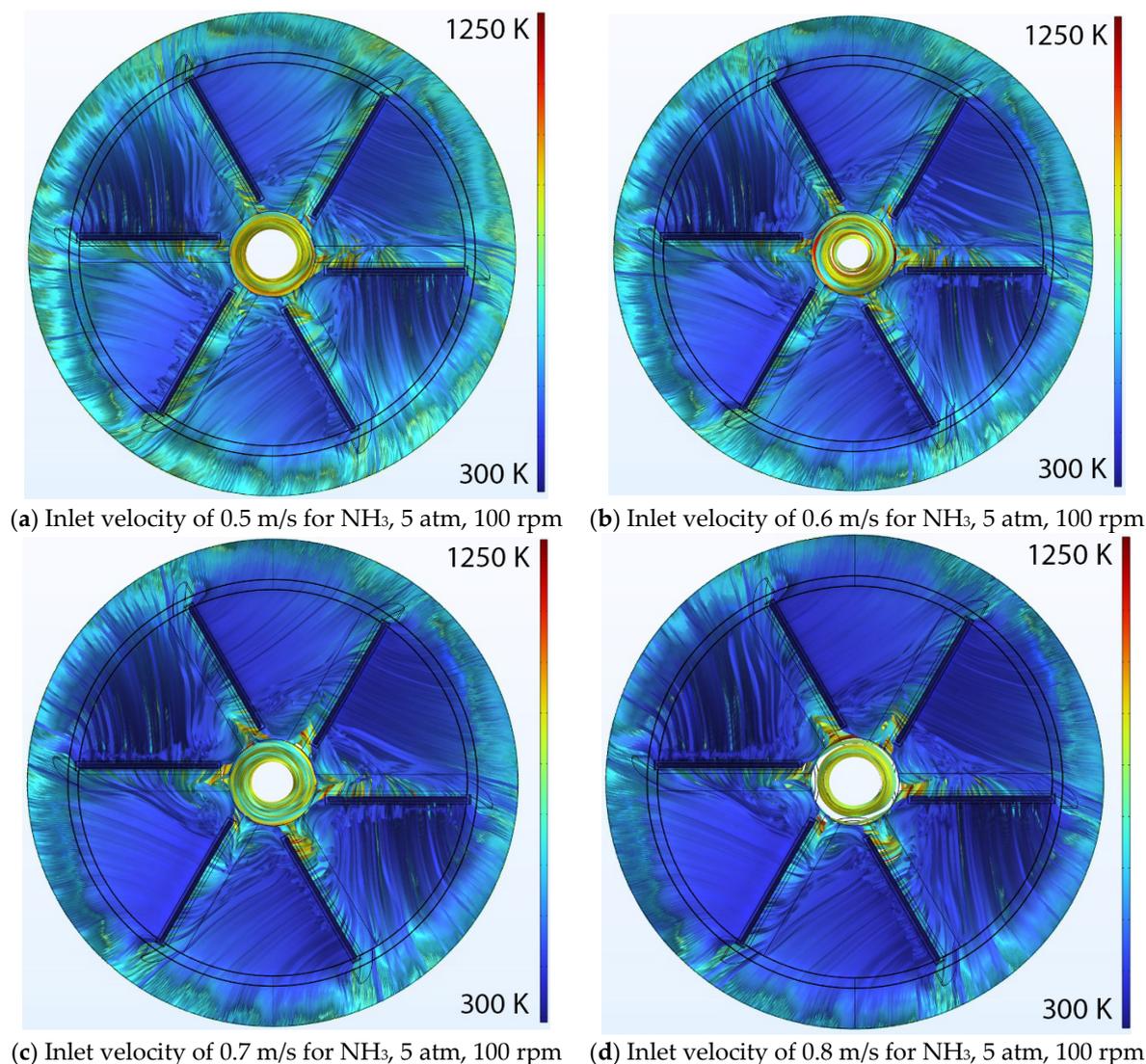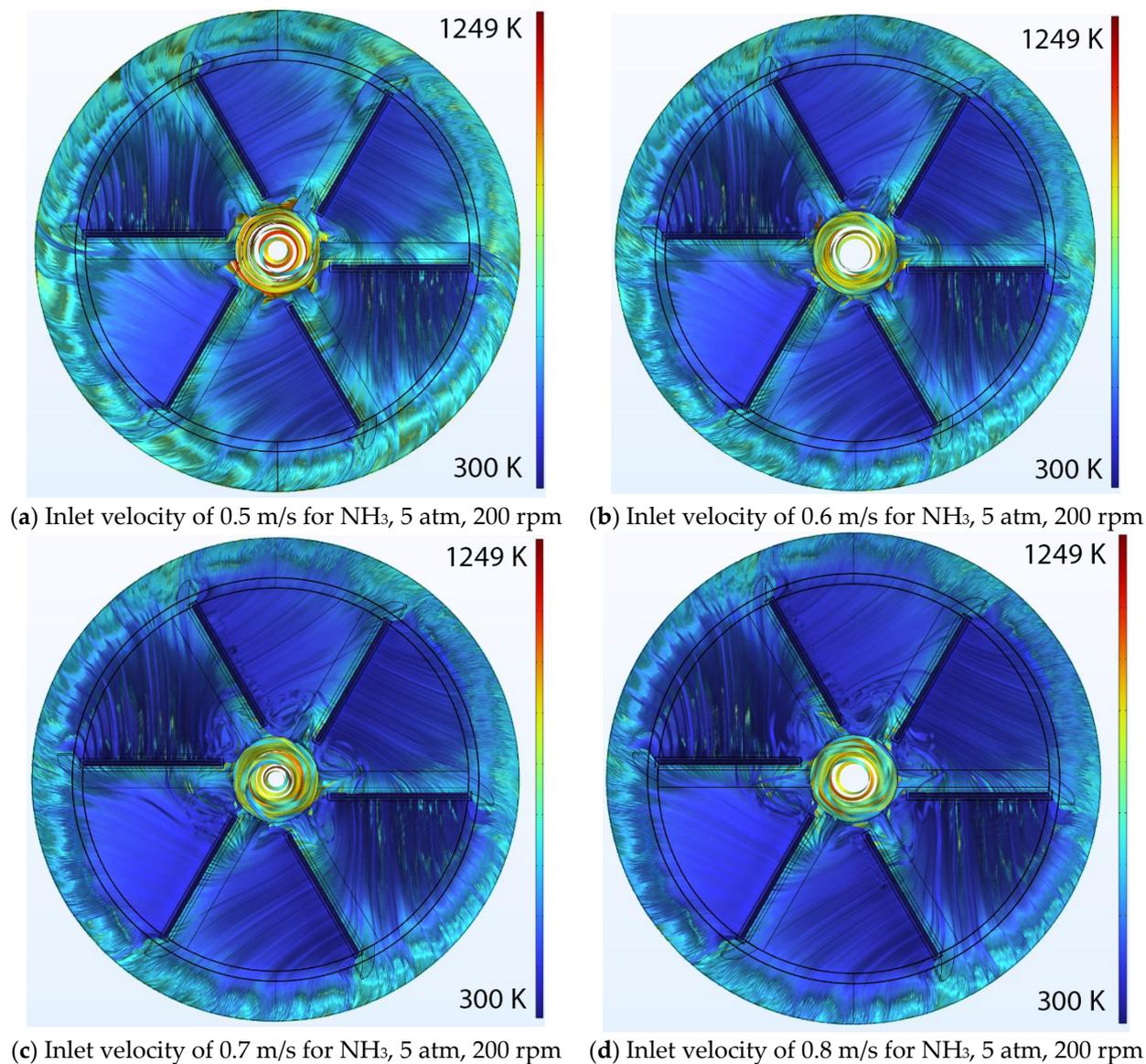
Figure 9. A top-down depiction showing 10,000 velocity streamlines color-coded according to temperature within the chambers, under the conditions of NH_3 at 5 atm pressure. The disk rotates at 200 rpm, while gas is introduced at inlet velocities of (**a**) 0.5 m/s, (**b**) 0.6 m/s, (**c**) 0.7 m/s, and (**d**) 0.8 m/s. Gas temperature is consistently color-coded across all panels, varying from 300 K (blue) to 1249 K (red).

As observed in Table 5, an inlet velocity of 0.8 m/s satisfies the criteria for ammonia at both operating pressures of 5 and 10 atm, albeit at different rotational speeds: 50 rpm and 100 rpm, respectively. Review of acceptable operating conditions for the other two gases suggests operating conditions that are communal to all three gases at the same time, suggesting this to be the desired operating state of the system if a generally stable system is desired regardless of what gas type or composition is being flown into each individual chamber (see Table 6 for a summary).

To operate the system with ammonia at pressures exceeding 10 atm, the ammonia would need to be blended with additional nitrogen and/or hydrogen. This act would lead to a fluid with properties determined by the ratio of the different gases. Review of the three gas characteristics suggest that while few overlapping conditions exist between the pure gases, suitable flow patterns with gas mixtures is possible at a wider range of operating conditions, though at unknown composition mixtures. Further studies on the impact of gas blends on the identification of suitable operating conditions is hence encouraged.

Table 6. Selected cases under which all gases simultaneously pass the passing/failing criterion, providing suitable operating conditions of the HPS-CVD reactor insensitive to the incoming gas type.

Pressure (atm)	Gas Types	Inlet Speed (m/s)	Rotational Speed (rpm)
5	N_2, H_2, NH_3	0.8	50
10	N_2, H_2, NH_3	0.8	100
20	N_2, H_2	0.8	300
30	N_2, H_2	0.7	400

6. Summary

This study presents 3D numerical simulations of a vertical high-pressure MOCVD reactor in COMSOL Multiphysics. The key goal of this paper is to determine the minimum gas inlet speed required at several high operating pressures inside the reactor to observe smooth/dominant vortex-free motion on top of wafers. The analysis of the results involved examining velocity streamlines on the X-Y plane in the numerical domain. For the fluid flow analysis, the influence of the inlet flow rate and the rotational speed of the carrier disk was investigated for three different working fluids: N_2, H_2, and NH_3 at four different operating pressures: 5, 10, 20, and 30 atm.

The analysis of the streamlines indicated that establishing a smooth gas flow pattern within the reactor requires a correlation between the rotational speed of the carrier disk and the inlet flow velocity. Consequently, a thorough and parametric study was conducted for each gas type to determine the minimum inlet velocity values at their respective rotational speeds, ensuring the attainment of a smooth flow pattern over the majority of the wafers' areas.

Based on the findings, it can be concluded that a minimum inlet velocity of 0.8 m/s is required for all three gases at 5 and 10 atm to simultaneously meet the specified passing criterion. At a pressure of 20 atm, an inlet velocity of 0.8 m/s and rotational speed of 300 rpm were needed to achieve smooth flow patterns on the surface of wafers. Similarly, for 30 atm, an inlet velocity of 0.7 m/s and rotational speed of 400 rpm were identified.

top-down depiction showing 10,000 velocity streamlines color-coded according to temperature within the chambers, under the conditions of N_2 at 30 atm pressure. The disk rotates at 200 rpm, while gas is introduced at inlet velocities of (a) 0.5 m/s, (b) 0.6 m/s, (c) 0.7 m/s, and (d) 0.8 m/s. Gas temperature is consistently color-coded across all panels, varying from 300 K (blue) to 1288 K (red); Figure S8. A top-down depiction showing 10,000 velocity streamlines color-coded according to temperature within the chambers, under the conditions of N_2 at 30 atm pressure. The disk rotates at 300 rpm, while gas is introduced at inlet velocities of (a) 0.5 m/s, (b) 0.6 m/s, (c) 0.7 m/s, and (d) 0.8 m/s. Gas temperature is consistently color-coded across all panels, varying from 300 K (blue) to 1257 K (red); Figure S9. A top-down depiction showing 10,000 velocity streamlines color-coded according to temperature within the chambers, under the conditions of N_2 at 30 atm pressure. The disk rotates at 400 rpm, while gas is introduced at inlet velocities of (a) 0.5 m/s, (b) 0.6 m/s, (c) 0.7 m/s, and (d) 0.8 m/s. Gas temperature is consistently color-coded across all panels, varying from 300 K (blue) to 1288 K (red); Figure S10. A top-down depiction showing 10,000 velocity streamlines color-coded according to temperature within the chambers, under the conditions of H_2 at 10 atm pressure. The disk rotates at 100 rpm, while gas is introduced at inlet velocities of (a) 0.5 m/s, (b) 0.6 m/s, (c) 0.7 m/s, and (d) 0.8 m/s. Gas temperature is consistently color-coded across all panels, varying from 300 K (blue) to 1306 K (red); Figure S11. A top-down depiction showing 10,000 velocity streamlines color-coded according to temperature within the chambers, under the conditions of H_2 at 10 atm pressure. The disk rotates at 200 rpm, while gas is introduced at inlet velocities of (a) 0.5 m/s, (b) 0.6 m/s, (c) 0.7 m/s, and (d) 0.8 m/s. Gas temperature is consistently color-coded across all panels, varying from 300 K (blue) to 1337 K (red); Figure S12. A top-down depiction showing 10,000 velocity streamlines color-coded according to temperature within the chambers, under the conditions of H_2 at 10 atm pressure. The disk rotates at 300 rpm, while gas is introduced at inlet velocities of (a) 0.5 m/s, (b) 0.6 m/s, (c) 0.7 m/s, and (d) 0.8 m/s. Gas temperature is consistently color-coded across all panels, varying from 300 K (blue) to 1350 K (red); Figure S13. A top-down depiction showing 10,000 velocity streamlines color-coded according to temperature within the chambers, under the conditions of H_2 at 20 atm pressure. The disk rotates at 200 rpm, while gas is introduced at inlet velocities of (a) 0.5 m/s, (b) 0.6 m/s, (c) 0.7 m/s, and (d) 0.8 m/s. Gas temperature is consistently color-coded across all panels, varying from 300 K (blue) to 1388 K (red); Figure S14. A top-down depiction showing 10,000 velocity streamlines color-coded according to temperature within the chambers, under the conditions of H_2 at 20 atm pressure. The disk rotates at 300 rpm, while gas is introduced at inlet velocities of (a) 0.5 m/s, (b) 0.6 m/s, (c) 0.7 m/s, and (d) 0.8 m/s. Gas temperature is consistently color-coded across all panels, varying from 300 K (blue) to 1355 K (red); Figure S15. A top-down depiction showing 10,000 velocity streamlines color-coded according to temperature within the chambers, under the conditions of H_2 at 20 atm pressure. The disk rotates at 400 rpm, while gas is introduced at inlet velocities of (a) 0.5 m/s, (b) 0.6 m/s, (c) 0.7 m/s, and (d) 0.8 m/s. Gas temperature is consistently color-coded across all panels, varying from 300 K (blue) to 1330 K (red); Figure S16. A top-down depiction showing 10,000 velocity streamlines color-coded according to temperature within the chambers, under the conditions of H_2 at 30 atm pressure. The disk rotates at 200 rpm, while gas is introduced at inlet velocities of (a) 0.5 m/s, (b) 0.6 m/s, (c) 0.7 m/s, and (d) 0.8 m/s. Gas temperature is consistently color-coded across all panels, varying from 300 K (blue) to 1330 K (red); Figure S17. A top-down depiction showing 10,000 velocity streamlines color-coded according to temperature within the chambers, under the conditions of H2 at 30 atm pressure. The disk rotates at 300 rpm, while gas is introduced at inlet velocities of (a) 0.5 m/s, (b) 0.6 m/s, (c) 0.7 m/s, and (d) 0.8 m/s. Gas temperature is consistently color-coded across all panels, varying from 300 K (blue) to 1350 K (red); Figure S18 A top-down depiction showing 10,000 velocity streamlines color-coded according to temperature within the chambers, under the conditions of H_2 at 30 atm pressure. The disk rotates at 400 rpm, while gas is introduced at inlet velocities of (a) 0.5 m/s, (b) 0.6 m/s, (c) 0.7 m/s, and (d) 0.8 m/s. Gas temperature is consistently color-coded across all panels, varying from 300 K (blue) to 1282 K (red); Figure S19. A top-down depiction showing 10,000 velocity streamlines color-coded according to temperature within the chambers, under the conditions of NH_3 at 10 atm pressure. The disk rotates at 200 rpm, while gas is introduced at inlet velocities of (a) 0.5 m/s, (b) 0.6 m/s, (c) 0.7 m/s, and (d) 0.8 m/s. Gas temperature is consistently color-coded across all panels, varying from 300 K (blue) to 1313 K (red); Figure S20. A top-down depiction showing 10,000 velocity streamlines color-coded according to temperature within the chambers, under the conditions of NH_3 at 10 atm pressure. The disk rotates at 300 rpm, while gas is introduced at inlet velocities of (a) 0.5 m/s, (b) 0.6 m/s, (c) 0.7 m/s, and (d) 0.8 m/s. Gas temperature is consistently color-coded across all panels, varying from 300 K (blue) to 1252 K (red); Figure S21. A top-down depiction showing 10,000 velocity streamlines color-coded

according to temperature within the chambers, under the conditions of NH$_3$ at 10 atm pressure. The disk rotates at 400 rpm, while gas is introduced at inlet velocities of (a) 0.5 m/s, (b) 0.6 m/s, (c) 0.7 m/s, and (d) 0.8 m/s. Gas temperature is consistently color-coded across all panels, varying from 300 K (blue) to 1212 K (red).

References

1. Flack, T.J.; Pushpakaran, B.N.; Bayne, S.B. GaN Technology for Power Electronic Applications: A Review. *J. Electron. Mater.* **2016**, *45*, 2673–2682. [CrossRef]
2. Scholz, F. MOVPE of Group-III Heterostructures for Optoelectronic Applications. *Cryst. Res. Technol.* **2020**, *55*, 1900027. [CrossRef]
3. Wang, C.A. Perspectives on the Development of Metalorganic Vapor Phase Epitaxy for III-V Optoelectronic Devices. *IEEE J. Quantum Electron.* **2022**, *58*, 1–11. [CrossRef]
4. Wang, C.A. Early History of MOVPE Reactor Development. *J. Cryst. Growth* **2019**, *506*, 190–200. [CrossRef]
5. Irvine, S.; Capper, P. (Eds.) *Metalorganic Vapor Phase Epitaxy (MOVPE)*; Wiley: Hoboken, NJ, USA, 2019; ISBN 9781119313014.
6. Pimputkar, S.; Speck, J.S.; DenBaars, S.P.; Nakamura, S. Prospects for LED Lighting. *Nat. Photonics* **2009**, *3*, 180–182. [CrossRef]
7. MacChesney, J.B.; Bridenbaugh, P.M.; O'Connor, P.B. Thermal Stability of Indium Nitride at Elevated Temperatures and Nitrogen Pressures. *Mater. Res. Bull.* **1970**, *5*, 783–791. [CrossRef]
8. Yamamoto, A.; Sugita, K.; Hashimoto, A. Elucidation of Factors Obstructing Quality Improvement of MOVPE-Grown InN. *J. Cryst. Growth* **2009**, *311*, 4636–4640. [CrossRef]
9. Lymperakis, L.; Schulz, T.; Freysoldt, C.; Anikeeva, M.; Chen, Z.; Zheng, X.; Shen, B.; Chèze, C.; Siekacz, M.; Wang, X.Q.; et al. Elastically Frustrated Rehybridization: Origin of Chemical Order and Compositional Limits in InGaN Quantum Wells. *Phys. Rev. Mater.* **2018**, *2*, 011601. [CrossRef]
10. Ivanov, S.V.; Shubina, T.V.; Komissarova, T.A.; Jmerik, V.N. Metastable Nature of InN and In-Rich InGaN Alloys. *J. Cryst. Growth* **2014**, *403*, 83–89. [CrossRef]
11. Borovac, D.; Sun, W.; Peart, M.R.; Song, R.; Wierer, J.J.; Tansu, N. Low Background Doping in AlInN Grown on GaN via Metalorganic Vapor Phase Epitaxy. *J. Cryst. Growth* **2020**, *548*, 125847. [CrossRef]
12. Miyoshi, M.; Yamanaka, M.; Egawa, T.; Takeuchi, T. Microstructure Variation in Thick AlInN Films Grown on C-Plane GaN on Sapphire by Metalorganic Chemical Vapor Deposition. *J. Cryst. Growth* **2019**, *506*, 40–44. [CrossRef]
13. Sangiovanni, D.G.; Gueorguiev, G.K.; Kakanakova-Georgieva, A. Ab Initio Molecular Dynamics of Atomic-Scale Surface Reactions: Insights into Metal Organic Chemical Vapor Deposition of AlN on Graphene. *Phys. Chem. Chem. Phys.* **2018**, *20*, 17751–17761. [CrossRef] [PubMed]
14. Sangiovanni, D.G.; Faccio, R.; Gueorguiev, G.K.; Kakanakova-Georgieva, A. Discovering Atomistic Pathways for Supply of Metal Atoms from Methyl-Based Precursors to Graphene Surface. *Phys. Chem. Chem. Phys.* **2022**, *25*, 829–837. [CrossRef] [PubMed]
15. Freitas, R.R.Q.; Gueorguiev, G.K.; De Brito Mota, F.; De Castilho, C.M.C.; Stafström, S.; Kakanakova-Georgieva, A. Reactivity of Adducts Relevant to the Deposition of Hexagonal BN from First-Principles Calculations. *Chem. Phys. Lett.* **2013**, *583*, 119–124. [CrossRef]
16. Stringfellow, G.B. Fundamental Aspects of Organometallic Vapor Phase Epitaxy. *Mater. Sci. Eng. B* **2001**, *87*, 97–116. [CrossRef]
17. Woods, V.T. *High Pressure Chemical Vapor Deposition: A Novel Approach for the Growth of Indium Nitride*; Georgia State University: Atlanta, Georgia, 2006.
18. Dietz, N. Real-Time Optical Characterization of Thin Film Growth. *Mater. Sci. Eng. B* **2001**, *87*, 1–22. [CrossRef]
19. Dietz, N.; Alevli, M.; Kang, H.; Strassburg, M.; Woods, V.; Ferguson, I.T.; Moore, C.E.; Cardelino, B.H. The Growth of InN and Related Alloys by High-Pressure CVD. In *Operational Characteristics and Crystal Growth of Nonlinear Optical Materials II*; SPIE: Bellingham, WA, USA, 2005; Volume 5912, pp. 78–85. [CrossRef]
20. Dietz, N. High Pressure Chemical Vapor Deposition Apparatuses, Methods, and Compositions Produced Therewith. European Patent EP2464760A4, 2013. Available online: https://patents.google.com/patent/WO2011019920A1/de (accessed on 20 March 2024).

21. Alevli, M.; Durkaya, G.; Weerasekara, A.; Perera, A.G.U.; Dietz, N.; Fenwick, W.; Woods, V.; Ferguson, I. Characterization of InN Layers Grown by High-Pressure Chemical Vapor Deposition. *Appl. Phys. Lett.* **2006**, *89*, 1023–1026. [CrossRef]

22. Indika Senevirathna, M.K.; Gamage, S.; Atalay, R.; Acharya, A.R.; Unil Perera, A.G.; Dietz, N.; Buegler, M.; Hoffmann, A.; Su, L.; Melton, A.; et al. Effect of Reactor Pressure on the Electrical and Structural Properties of InN Epilayers Grown by High-Pressure Chemical Vapor Deposition. *J. Vac. Sci. Technol. A Vac. Surf. Film.* **2012**, *30*, 031511. [CrossRef]

23. Yousefian, P.; Pimputkar, S. Computational Fluid Dynamics Modeling of a New High-Pressure Chemical Vapor Deposition Reactor Design. *J. Cryst. Growth* **2021**, *566–567*, 126155. [CrossRef]

24. Papavasileiou, P.; Koronaki, E.D.; Pozzetti, G.; Kathrein, M.; Czettl, C.; Boudouvis, A.G.; Mountziaris, T.J.; Bordas, S.P.A. An Efficient Chemistry-Enhanced CFD Model for the Investigation of the Rate-Limiting Mechanisms in Industrial Chemical Vapor Deposition Reactors. *Chem. Eng. Res. Des.* **2022**, *186*, 314–325. [CrossRef]

25. Theodoropoulos, C.; Mountziaris, T.J.; Moffat, H.K.; Han, J. Design of Gas Inlets for the Growth of Gallium Nitride by Metalorganic Vapor Phase Epitaxy. *J. Cryst. Growth* **2000**, *217*, 65–81. [CrossRef]

26. Barua, H.; Povitsky, A. Numerical Model of Carbon Chemical Vapor Deposition at Internal Surfaces. *Vacuum* **2020**, *175*, 109234. [CrossRef]

27. Psarellis, G.M.; Aviziotis, I.G.; Duguet, T.; Vahlas, C.; Koronaki, E.D.; Boudouvis, A.G. Investigation of Reaction Mechanisms in the Chemical Vapor Deposition of al from DMEAA. *Chem. Eng. Sci.* **2018**, *177*, 464–470. [CrossRef]

28. Zou, S.; Xiao, J.; Wu, V.; Chen, X.D. Analyzing Industrial CVD Reactors Using a Porous Media Approach. *Chem. Eng. J.* **2021**, *415*, 129038. [CrossRef]

29. Cheimarios, N.; Kavousanakis, M.; Kokkoris, G.; Boudouvis, A.G. Beware of Symmetry Breaking and Periodic Flow Regimes in Axisymmetric CVD Reactor Setups. *Comput. Chem. Eng.* **2019**, *124*, 124–132. [CrossRef]

30. Wu, Y.; Wu, R.; Zhou, X.; Wang, H.; Hu, Y.; Nie, D.; Bao, D. Numerical Modelling on the Effect of Temperature on MOCVD Growth of ZnO Using Diethylzinc and Tertiarybutanol. *Coatings* **2022**, *12*, 1991. [CrossRef]

31. Huang, Z.; Qie, S.; Quan, X.; Guo, K.; Liu, C. Numerical Simulation of Multiple Polysilicon CVD Reactors Connected in Series Using CFD Method. *Can. J. Chem. Eng.* **2015**, *93*, 1721–1729. [CrossRef]

32. Ni, H.; Lu, S.; Chen, C. Modeling and Simulation of Silicon Epitaxial Growth in Siemens CVD Reactor. *J. Cryst. Growth* **2014**, *404*, 89–99. [CrossRef]

33. Gakis, G.P.; Koronaki, E.D.; Boudouvis, A.G. Numerical Investigation of Multiple Stationary and Time-Periodic Flow Regimes in Vertical Rotating Disc CVD Reactors. *J. Cryst. Growth* **2015**, *432*, 152–159. [CrossRef]

34. Raj, E.; Lisik, Z.; Niedzielski, P.; Ruta, L.; Turczynski, M.; Wang, X.; Waag, A. Modelling of MOCVD Reactor: New 3D Approach. *J. Phys. Conf. Ser.* **2014**, *494*, 012019. [CrossRef]

35. Lin, C.H.; Cheng, W.T.; Lee, J.H. Effect of Embedding a Porous Medium on the Deposition Rate in a Vertical Rotating MOCVD Reactor Based on CFD Modeling. *Int. Commun. Heat Mass Transf.* **2009**, *36*, 680–685. [CrossRef]

36. Sytniewski, Ł.J.; Lapkin, A.A.; Stepanov, S.; Wang, W.N. CFD Optimisation of Up-Flow Vertical HVPE Reactor for GaN Growth. *J. Cryst. Growth* **2008**, *310*, 3358–3365. [CrossRef]

37. Tabatabaei, S. *Evaluation of Fluid Dynamic Effect on Thin Film Growth in a Horizontal Type Meso-Scale Chemical Vapor Deposition Reactor Using Computational Fluid Dynamics*; University of Alabama: Tuscaloosa, AL, USA, 2013.

38. Kempisty, P.; Łucznik, B.; Pastuszka, B.; Grzegory, I.; Boćkowski, M.; Krukowski, S.; Porowski, S. CFD and Reaction Computational Analysis of the Growth of GaN by HVPE Method. *J. Cryst. Growth* **2006**, *296*, 31–42. [CrossRef]

39. Bao, Q.; Zhu, T.; Zhou, N.; Guo, S.; Luo, J.; Zhao, C. Effect of Hydrogen Carrier Gas on AlN and AlGaN Growth in AMEC Prismo D-Blue®MOCVD Platform. *J. Cryst. Growth* **2015**, *419*, 52–56. [CrossRef]

40. Li, Z.; Li, H.; Zhang, J.; Li, J.; Jiang, H.; Fu, X.; Han, Y.; Xia, Y.; Huang, Y.; Yin, J.; et al. A Susceptor with Partial-Torus Groove in Vertical MOCVD Reactor by Induction Heating. *Int. J. Heat Mass Transf.* **2014**, *75*, 410–413. [CrossRef]

41. Fu, K.; Fu, Y.; Han, P.; Zhang, Y.; Zhang, R. Kinetic Monte Carlo Study of Metal Organic Chemical Vapor Deposition Growth Dynamics of GaN Thin Film at Microscopic Level. *J. Appl. Phys.* **2008**, *103*, 103524. [CrossRef]

42. Shinde, V.M.; Deivendran, B.; Kumar, H.; Eswara Prasad, N. Investigation of Transport Processes in a Commercial Hot Wall CVD Reactor with Multi-Substrates for High-Quality Pyrocarbon Deposition. *Surf. Coat. Technol.* **2021**, *425*, 127685. [CrossRef]

43. Chuang, Y.C.; Chen, C.T. Mathematical Modeling and Optimal Design of an MOCVD Reactor for GaAs Film Growth. *J. Taiwan Inst. Chem. Eng.* **2014**, *45*, 254–267. [CrossRef]

44. Gkinis, P.A.; Aviziotis, I.G.; Koronaki, E.D.; Gakis, G.P.; Boudouvis, A.G. The Effects of Flow Multiplicity on GaN Deposition in a Rotating Disk CVD Reactor. *J. Cryst. Growth* **2017**, *458*, 140–148. [CrossRef]

45. He, Y.; Wang, J.; Luo, T.; Pei, Y. Analysis and Optimization of MOCVD Flow Ratio Based on Machine Learning and PSO Algorithm. *J. Cryst. Growth* **2022**, *590*, 126683. [CrossRef]

46. Enayati, H.; Pimputkar, S. Computational Fluid Dynamic Analysis of a High-Pressure Spatial Chemical Vapor Deposition (HPS-CVD) Reactor for Flow Stability. *Crystals* **2024**, *14*, 105. [CrossRef]

47. COMSOL Multiphysics. Available online: https://www.comsol.com/ (accessed on 20 June 2023).

48. Span, R.; Lemmon, E.W.; Jacobsen, R.T.; Wagner, W.; Yokozeki, A. A Reference Equation of State for the Thermodynamic Properties of Nitrogen for Temperatures from 63.151 to 1000 K and Pressures to 2200 MPa. *J. Phys. Chem. Ref. Data* **2000**, *29*, 1361–1401. [CrossRef]

49. Leachman, J.W.; Jacobsen, R.T.; Penoncello, S.G.; Lemmon, E.W. Fundamental Equations of State for Parahydrogen, Normal Hydrogen, and Orthohydrogen. *J. Phys. Chem. Ref. Data* **2009**, *38*, 721–748. [CrossRef]
50. Tillner-Roth, R.; Harms-Watzenberg, F.; Baehr, H.D. *A New Fundamental Equation for Ammonia; Eine Neue Fundamentalgleichung Fuer Ammoniak*; Germany. 1994. Available online: https://www.osti.gov/etdeweb/biblio/42394 (accessed on 20 March 2024).
51. Monogenidou, S.A.; Assael, M.J.; Huber, M.L. Reference Correlation for the Viscosity of Ammonia from the Triple Point to 725 K and up to 50 MPa. *J. Phys. Chem. Ref. Data* **2018**, *47*, 023102. [CrossRef] [PubMed]